

Journal of Materials Chemistry A

Accepted Manuscript



This is an *Accepted Manuscript*, which has been through the Royal Society of Chemistry peer review process and has been accepted for publication.

Accepted Manuscripts are published online shortly after acceptance, before technical editing, formatting and proof reading. Using this free service, authors can make their results available to the community, in citable form, before we publish the edited article. We will replace this *Accepted Manuscript* with the edited and formatted *Advance Article* as soon as it is available.

You can find more information about *Accepted Manuscripts* in the [Information for Authors](#).

Please note that technical editing may introduce minor changes to the text and/or graphics, which may alter content. The journal's standard [Terms & Conditions](#) and the [Ethical guidelines](#) still apply. In no event shall the Royal Society of Chemistry be held responsible for any errors or omissions in this *Accepted Manuscript* or any consequences arising from the use of any information it contains.

Controllable growth of graphene/Cu composite and its nanoarchitecture-dependent electrocatalytic activity to hydrazine oxidation

Chengbin Liu,^{*a} Hang Zhang,^a Yanhong Tang^b and Shenglian Luo^{*a}

Received (in XXX, XXX) Xth XXXXXXXXXX 20XX, Accepted Xth XXXXXXXXXX 20XX

DOI: 10.1039/b000000x

Graphene is a promising support for nanosized electrocatalysts, while conventional stacking arrangement of graphene sheets substantially decreases the catalytic sites on the catalysts. We report here the fabrication of graphene/Cu electrocatalyst by simple cyclic voltammetric electrolysis of graphene oxide (GO) and copper ethylenediamine tetraacetate (Cu-EDTA), and find that the electrochemically reduced GO (RGO) and Cu nanoparticles can be sequentially self-assembled into layer-by-layer, 3D sandwich-type, and homogenous architectures as the concentration ratio of Cu-EDTA/GO increases. The 3D sandwich-type RGO/Cu composite (S-RGO/Cu) shows that the RGO sheets decorated with Cu nanoparticles nearly stand on the electrode, leading to a significant increase of electrochemically accessible surface area (0.685 cm^2) relative to those of the horizontal layer-by-layer RGO/Cu composite (0.147 cm^2) and the homogenous RGO/Cu composite (0.265 cm^2). Stemming from its high electrochemical surface area, the S-RGO/Cu composite exhibits a high electrocatalytic activity to hydrazine oxidation in terms of current density and overpotential. Mechanistic analysis of the electrode reactions reveals the reaction pathways of hydrazine on RGO/Cu are closely related to the electrochemical surface area of the RGO/Cu electrocatalyst. The correlation between the architectures and their performances in electrocatalysis presented can guide the design of the novel structures with enhanced properties.

1. Introduction

Electrocatalysts are the key component in the applications such as electrochemical sensors, fuel cells, and electrochemical hydrogen evolution reactions.¹⁻³ Supporting materials with a large specific surface area have been widely used to effectively disperse and stabilize the catalyst nanoparticles.^{4,5} Meanwhile, maximizing the electrochemically active area of the catalyst is pursued to enhance the catalytic activity.^{6,7} Recently graphene (mainly reduced graphene oxide, RGO) has quickly emerged as a superior catalyst support^{8,9} because of its unique structure and properties, including high specific surface area, excellent electrical conductivity, great mechanical and chemical stability, strong nanoparticle anchoring, and also good electrocatalytic activity.^{10,11} Up to now, although tremendous progress has been achieved in preparation of RGO/metal (Au, Ag, Pt, Pd, bi-/multi-metallic) catalysts,¹²⁻¹⁵ most of them obtained by chemical solution methods macroscopically exist in powder aggregates, so they have to be coated onto an electrode substrate under the assist of a polymeric binder. As a result, the catalytic activity may be severely impaired by the binder due to the entrapment of a substantial amount of catalytic sites.

Electrodeposition enables a facile fabrication of firmly adherent binder-free electrocatalysts on a conductive substrate in only one step and moreover an easy control in morphology/structure, making it a favourable method for electrocatalyst fabrication.^{16,17} We recently proposed direct electrodeposition of RGO from graphene oxide (GO) aqueous solutions^{18,19} and then we demonstrated facile functionalization of the RGO films by co-depositing RGO with materials of interest onto electrodes,²⁰⁻²³ opening a new opportunity for a simple, rapid, and environmentally friendly production of functional graphene-based nanocomposites for use in various fields including electrocatalysis.²⁴⁻²⁷ The performance of RGO as a catalyst support, however, has yet to be significantly improved because the RGO sheets tend to horizontally stack on electrodes^{20,24,27} due to

the intersheet van der Waals attractions, which may result in a significant loss in the electrochemical surface area of the electrocatalysts because of their confinement within the RGO layers.

In this work, we demonstrate that RGO sheets not only can horizontally stack but also can stand on an electrode during a simple one-step cyclic voltammetric (CV) electrodeposition in the presence of metal, herein copper nanoparticles. Copper (Cu) is an important catalyst/co-catalyst in electrochemical sensors (e.g., detection of glucose,²⁸ hydrazine,²⁹ etc.) and fuel cells^{30–32} owing to its low cost. Just by varying the initial concentrations of the cupreous precursor during CV electrodeposition of the RGO/Cu, three architectures: layer-by-layer (L-), sandwich-like (S-), and homogeneous (H-) structures are obtained (Scheme 1). In the S-RGO/Cu composite, the RGO sheets act as scaffolds to support Cu nanoparticles to form sandwich-like RGO/Cu sheets nearly standing on the electrode surface, preventing the stacking of RGO and providing a high surface electrochemically accessible to electrolytes. The growth mechanisms are tentatively given for the three nanoarchitectures of RGO/Cu and the correlations between the nanoarchitectures and the performances in hydrazine (N₂H₄) electro-oxidation are investigated.

2. Experimental section

2.1 Electrochemical preparation of RGO/Cu composite

Graphite oxide was prepared according to our previous work.²¹ The synthesized graphite oxide powder was exfoliated in a 0.067 M pH=8 phosphate buffer solution (PBS) by ultrasonication for 3 h to form a homogeneous GO dispersion. Equimolar quantities of CuSO₄ and disodium ethylenediamine tetraacetate (Na-EDTA) were mixed to obtain a Cu-EDTA solution. For electrodeposition preparation of RGO/Cu, dispersions containing 0.3 g L⁻¹ GO and Cu-EDTA with varied concentrations were prepared. The electrodeposition was carried out under magnetic stirring using cyclic voltammetry on a CHI 660C electrochemical workstation (CH Instruments, Shanghai,

China) with a three-electrode system: a glassy carbon electrode (GCE) (3 mm in diameter, 0.071 cm² in geometric area) as the working electrode, Pt foil as the counter electrode, and a saturated calomel electrode (SCE) as the reference electrode. Prior to use, the GCEs were carefully polished with 0.3 and subsequently 0.05 μm alumina slurry, and then cleaned by ultrasound in double-distilled water and ethanol for 2 min, respectively. The scans were performed between -1.4 and 0.6 V at the rate of 50 mV s⁻¹ for 10 cycles. After electrodeposition, the working electrode was thoroughly washed with double-distilled water and dried at room temperature. For comparison, neat RGO and neat Cu nanoparticles on GCEs were separately prepared under the same conditions.

2.2 Characterizations

Scanning electron microscopic (SEM) images were acquired using a Hitachi S-4800 field emission electron microscope. Transmission electron microscopic (TEM) images were obtained using a JEM 3010 TEM system. Powder X-ray diffraction (XRD) patterns were obtained on a M21X X-ray diffractometer with Cu Kα radiation ($\lambda = 1.54 \text{ \AA}$). Raman spectra were measured using an Advantage 200A Raman spectrometer with a 632.8 nm laser (DeltaNu). X-ray photoemission spectroscopy (XPS) data were recorded on a Thermo Fisher Scientific K-Alpha 1063 system with a monochromatic Al Kα source (1486.6 eV).

2.3 Electrochemical tests

The tests of electrocatalytic activity were performed using 10 mM N₂H₄ in 0.1 M KOH solution without being purged with N₂ (the result is not affected by the aeration of N₂ or not). The cyclic voltammograms of N₂H₄ electro-oxidation at the catalytic electrodes were adopted when the current responses stabilized (generally the second or more cycle). All the electrochemical tests were recorded on the CHI 660C electrochemical workstation at room temperature.

3. Results and discussion

3.1 Synthesis and structural characterization

The one-pot electrochemical synthesis of RGO/metal composites from GO and metallic precursors requires GO and the corresponding metallic precursor forming a homogeneous dispersion. We previously showed²⁰ that metallic anion species could stably coexist with GO due to the negative electrostatic repulse between them, but metallic cations, such as Ni^{2+} , Cu^{2+} , and Zn^{2+} could combine with negatively charged GO through strong electrostatic attraction to induce the agglomeration of GO in water, which disables the electrodeposition of RGO and thus the fabrication of corresponding RGO/metal composites. Herein, this problem is solved by introducing a chelating agent, ethylenediamine tetraacetate (EDTA), to chelate Cu^{2+} before its mixing with GO. As a result, the positive charge of free Cu^{2+} ionized from the CuSO_4 precursor is eliminated by EDTA and the resulting electrically neutral Cu-EDTA complex can well co-exist with GO in aqueous solutions at any concentration. EDTA chelates with metal ions in a 1:1 ratio regardless of the charge of the cation³³ and therefore in each electrolysis experiment, an electrolytic solution containing equimolar quantities of CuSO_4 and EDTA followed by GO addition (achieving a final GO concentration of 0.3 g L^{-1}) was prepared for fabricating RGO/Cu composite, where the concentrations of CuSO_4 were varied to investigate the morphologies of the RGO/Cu composite.

The SEM image in Fig. 1a displays the pure RGO film with a few wrinkles lying flat on a GCE, where the electrochemical reduction of GO to RGO has been well documented in our previous work.^{18–20} Raman and XPS spectra also confirmed the efficient removal of the oxygenated groups of GO during the electrodeposition process (Fig. S1 in Electronic Supplementary Information (ESI) †). Cu nanoparticles prepared from 1 mM Cu-EDTA without GO are shown in Fig. 1b, demonstrating an average diameter of about 22 nm and densely spreading on the electrode surface. RGO/Cu composite presented three typical morphologies depending on the concentration of Cu^{2+} ($[\text{Cu}^{2+}]$). Fig. 1c shows the SEM image of the RGO/Cu composite electrochemically deposited from 1 mM $[\text{Cu}^{2+}]$

and 0.3 g L^{-1} GO, demonstrating ultrathin and flexible RGO sheets covering the dense Cu nanoparticles. The flat RGO sheets as the topmost layer was always observed for this RGO/Cu composite irrespective of the electrodeposition cycle numbers (Fig. S2, ESI†). This reminds us that a layer-by-layer structure revealed in our earlier work^{20,21} is also present here (illustrated in Scheme 1a), which was attributed by us to the independent deposition of the two components due to no attractive interaction between them as well as their significantly different electrodeposition potentials. Here the reduction peak potentials for GO and Cu^{2+} also differ greatly to be -1.2 and -0.3 V (versus SCE), respectively (Fig. S3, ESI†) and the attractive interaction between the negatively charged GO and the neutral Cu-EDTA at lower concentrations could be neglected. According to our previous work,^{20,21} the growth mechanism for the layer-by-layer structure is illustrated in Scheme 2a. During the negative scan from 0.6 to -1.4 V the Cu nanoparticles first deposit alone at about -0.3 V and till to about -1.2 V the RGO deposition occurs, resulting in planar RGO sheets like blankets covering the predeposited Cu nanoparticles. Since the positive scan (from -1.4 to 0.6 V) results in no deposition, the repeated CV scans give rise to multiple RGO/Cu bilayers, as if layer-by-layer assembly of RGO and Cu nanoparticles, where RGO always constitutes the topmost layer as was observed in the experiments (Fig. S2, ESI†). Indeed, the layered structure was verified by cross-sectional SEM examination (Fig. 1d).

However, the layer-by-layer RGO/Cu (L-RGO/Cu) composite only can be found at low concentrations of Cu^{2+} up to about 3 mM . As the $[\text{Cu}^{2+}]$ further increases, a choppy morphology different from the flat L-RGO/Cu composite is observed (Fig. 1e), and a magnified SEM image (Fig. 1f) reveals RGO sheets sandwiched by dense Cu nanoparticles are nearly vertically standing on the electrode surface (as illustrated in Scheme 1b), forming a three-dimensional (3D) nanoarchitecture. Obviously, the electrodeposition mechanism for the 3D sandwich-type RGO/Cu (S-RGO/Cu) changed, and differing from the independent deposition of RGO and Cu inferred for the L-RGO/Cu

structure, simultaneous deposition of the two components could take place in this case. We deduce that, as illustrated in Scheme 2b, at the higher $[\text{Cu}^{2+}]$, each GO sheet was surrounded by Cu-EDTA and therefore GO would be entrained during the Cu-nanoparticle deposition at around -0.3 V, and meanwhile the 2D GO sheets that have various oxygen functional groups (e.g., hydroxyl and carboxyl groups) provided anchor sites for nucleation and growth of Cu nanoparticles at the GO surfaces.^{34,35} The GO scaffolds were subsequently electrochemically reduced to RGO at the cathodic potential of around -1.2 V. To our best knowledge, though 2D sandwich-like graphene-based nanocomposite sheets have been chemically prepared in solutions,^{36,37} the in situ assembly of the sandwich units on a solid support has never been reported. The RGO/nanoparticle sandwich sheets standing on the electrode surface constitute a 3D architecture, overcoming the consistent horizontal stack of RGO induced by intersheet van der Waals attractions, which will endow the composite with not only a large interface to facilitate the fast charge transport between the nanoparticles and the electrically conductive RGO but also a large electrochemically accessible surface area propitious to reactions. The binder-free, open structure and higher electrochemically accessible surface are great advantages for any electrocatalytic applications.^{38,39}

Further increasing the $[\text{Cu}^{2+}]$ to above 8 mM, a flat morphology with only close-packed Cu particles is observed from the top-view SEM image (Fig. 1g), and the cross-sectional SEM image reveals that RGO sheets are still sandwiched between Cu nanoparticles (Fig. 1h), indicating that such a structure was developed from the S-RGO/Cu shown in Fig. 1e and Fig. 1f. It is thought that in the electrolyte solution the GO sheets were surrounded by a crowd of Cu-EDTA due to the higher concentration ratio of Cu-EDTA to GO than that in the case of S-RGO/Cu preparation, and as illustrated in Scheme 2c, upon the negative scan to around -0.3 V, a mass of Cu^{2+} instantly reduced to form Cu nanoparticles and during their deposition onto the electrode the GO sheets were entrained, leading to the embedment of GO in the Cu-nanoparticle matrix. In this case, the high-

density Cu nanoparticles not only completely saturated the anchor sites on the GO sheets but also nucleated and grew on the electrode substrate. The GO sheets were then reduced to RGO as the potential went negatively to the potential of -1.2 V, giving birth to the RGO/Cu composite. And in this sense, RGO sheets play a role of nano-fillers that homogeneously distribute in the continuous Cu-nanoparticle matrix (H-RGO/Cu composite, hereafter).

The TEM images of the three types of RGO/Cu composites are shown in Fig. 2a–c, all revealing Cu nanoparticles with a diameter of 20 to 30 nm (comparable to that of the neat Cu nanoparticles in Fig. 1b) on a flexible and transparent substrate ascribed to RGO sheets that most likely contain more than one RGO monolayer. The Cu nanoparticles are anchored on the RGO sheets but they are sparse for the L-RGO/Cu (Fig. 2a), dense for the S-RGO/Cu (Fig. 2b), and crowded for the H-RGO/Cu (Fig. 2c), consistent with the successively increased concentrations of the cupreous precursor used for their preparations. The RGO/Cu composites were characterized by XRD (Fig. 2d–f). Besides the diffraction peaks at 2θ values of 43.30° , 50.44° , and 74.20° characteristic of cubic Cu (JCPDS file no. 85-1326),^{40,41} diffraction peaks indicative of Cu_2O (JCPDS file no. 05-0667) and CuO (JCPDS file no. 05-0661) are also present, suggesting partial oxidation of the Cu nanoparticles, especially in the S-RGO/Cu and H-RGO/Cu composites because they have most of the Cu nanoparticles exposed, so that the peaks for the oxides of copper in S-RGO/Cu and H-RGO/Cu is prominent relative to L-RGO/Cu. XPS also confirmed the partial oxidation of Cu in the three types of RGO/Cu composites (Fig. S4, ESI†). It has been reported that the oxides of copper (i.e., Cu_2O and CuO), which normally form on the outer layer of Cu nanoparticles, are not harmful but favorable for the electrocatalytic activity of Cu nanoparticles.^{30,42}

3.2 Electrocatalytic activity to N_2H_4

The electrocatalytic activities of L-RGO/Cu, S-RGO/Cu, and H-RGO/Cu composites towards N_2H_4 were examined using cyclic voltammetry. The CV curves of the GCEs of equivalent geometric areas

(0.071 cm^2) loaded with L-RGO/Cu, S-RGO/Cu, and H-RGO/Cu catalysts in 0.1 M KOH containing 10 mM N_2H_4 at the scan rate of 100 mV s^{-1} are displayed in Fig. 3, and at the same time a bare GCE and the GCEs separately loaded with Cu nanoparticles and RGO were also investigated for comparison. On the forward positive potential sweep, it is found that the bare GCE gives no anodic peak, while the anodic current at RGO starts to increase at 0.1 V (versus SCE, similarly hereinafter) and then achieves the maximum peak current at approximately 0.63 V, indicating an electrocatalytic activity of RGO towards N_2H_4 oxidation, agreeing with the report by Wang et al.⁴³ Nevertheless, compared to RGO, Cu nanoparticle is more effective for the electrocatalytic oxidation of N_2H_4 deducing from the remarkable negative shift of the oxidation peak potential to 0.34 V and the distinct increase of oxidation peak current density at the Cu catalyst. The electrocatalytic activities differ significantly for the three types of RGO/Cu composites, where the L-RGO/Cu composite exhibits a similar electrocatalytic N_2H_4 activity to that of Cu nanoparticles in terms of the peak current density (about 9.1 mA cm^{-2} for both), which suggests that the electrocatalytic activity of RGO toward N_2H_4 is negligible when in the presence of Cu nanoparticles. Still and all, the fact that the oxidation peak potential at L-RGO/Cu (0.27 V) is lower than that at Cu (0.34 V) imparts accelerated charge-transfer kinetics in L-RGO/Cu contributed by the electrically conductive RGO that facilitates electron transport.^{44,45} The peak current density observed for the S-RGO/Cu composite is 15.0 mA cm^{-2} , nearly two times that for the L-RGO/Cu, and moreover, the peak potential negatively shifts to 0.26 V. On the other hand, despite its higher Cu-nanoparticle content than that in the S-RGO/Cu composite, the H-RGO/Cu composite shows a decreased peak current of 11.0 mA cm^{-2} and an increased peak potential of 0.29 V. The results clearly indicate facile N_2H_4 electro-oxidation reaction on S-RGO/Cu compared to both L-RGO/Cu and H-RGO/Cu, which is supposed to be ascribed to the unique nanoarchitecture of the S-RGO/Cu composite. In S-RGO/Cu, the nearly standing RGO sheets acting as the scaffolds to support Cu nanoparticles maximizes the

surfaces of catalytical Cu nanoparticles available to N_2H_4 molecules. In the reverse negative potential scan, no cathodic peak is observed, suggesting irreversible oxidation of N_2H_4 on all the electrodes.

3.3 Effective surface area and electron transfer number

The electrochemically effective surface area of the electrodes can be estimated using $K_3[Fe(CN)_6]$ as a model complex according to the general Randles–Sevcik equation (Eq. 1):⁴⁶

$$i_p = (2.69 \times 10^5) n^{3/2} A c D^{1/2} \nu^{1/2} \quad (1)$$

where i_p , n , A , c , D and ν are the peak current (in A), the number of electrons (1 for $K_3[Fe(CN)_6]$) involved in the reaction, the electrochemically effective surface area of working electrode (in cm^2), the concentration of the reactant (in $mol\ cm^{-3}$), the diffusion coefficient ($7.6 \times 10^{-6}\ cm^2\ s^{-1}$ for $K_3[Fe(CN)_6]$), and the scan rate (in $V\ s^{-1}$), respectively. In consideration of that Cu nanoparticles in the RGO/Cu composite electrodes can react with $K_3[Fe(CN)_6]$, we only estimated the effective surface areas of the bare GCE and the RGO/GCE according to Eq. 1. From the slope of the anodic i_p versus $\nu^{1/2}$ plot (Fig. S5, ESI†) the electrochemically effective surface areas of the bare GCE and the RGO/GCE are calculated to be 0.059 and 0.135 cm^2 . It is known that the electrical double layer capacitance of an electrode is proportional to its effective electrode area according to Eq. 2:^{47–49}

$$C = \frac{\varepsilon A}{d} \quad (2)$$

where C is the capacitance, ε is permittivity of the electrolyte, d is effective thickness of the electrical double layer, and A is surface area of the electrode accessible to the electrolyte. Therefore, the effective surface areas of the RGO/Cu composite electrodes (A_x) can be evaluated according to Eq. 3 using the effective surface area (A_s , 0.135 cm^2) of the RGO/GCE electrode as a standard:

$$\frac{C_s}{C_x} = \frac{A_s}{A_x} \quad (3)$$

C_s and C_x can be evaluated based on cyclic voltammetry measurements using Eq. 4.⁵⁰⁻⁵²

$$C = \frac{1}{v} \frac{1}{\Delta V} \int IdV \quad (4)$$

where v is the potential scan rate, ΔV is the potential variation range, I is the instantaneous current, and $\int IdV$ is the voltammetric charge, which is numerically equal to the surrounded area of the voltammetric curve. Fig. S6 in the ESI† shows cyclic voltammograms for the bare GCE, RGO/GCE, Cu/GCE, L-RGO/Cu/GCE, S-RGO/Cu/GCE, and H-RGO/Cu/GCE in 0.1 M KOH without N_2H_4 at the scan rate of 0.1 V s^{-1} in the potential range of -0.4 – $+0.7 \text{ V}$. On the basis of the value of A_s (0.135 cm^2) for RGO/GCE, according to Eq. 3 and 4, the calculated effective area of bare GCE is 0.059 cm^2 , in excellent agreement with the value obtained using Eq. 1, meaning the proposed method for the evaluation of effective areas of the electrodes is reliable. Hence, the effective areas for the Cu-containing electrodes, Cu/GCE, L-RGO/Cu/GCE, S-RGO/Cu/GCE, and H-RGO/Cu/GCE, are similarly calculated to be 0.121 , 0.147 , 0.685 , and 0.265 cm^2 , respectively. The results reveal that the effective surface of GCE increases obviously after the electrode modification, and particularly the S-RGO/Cu composite electrode has the electrochemically effective surface area 4 times larger than that of the L-RGO/Cu composite electrode and 2 times larger than that of the H-RGO/Cu composite electrode.

The effect of scan rate (v) was then investigated in the range of 50 – 250 mV s^{-1} using $10 \text{ mM } N_2H_4$ in 0.1 M KOH for getting insight into the oxidation mechanism of N_2H_4 on the three composite electrodes (Fig. 4a1–a3). For comparison, the same investigations were conducted on the RGO and the Cu electrodes as well (Fig. S7a1 and a2, ESI†). In all the cases, the peak potentials shifted toward positive direction with increasing v , again indicating the oxidations of N_2H_4 on the electrodes are irreversible processes. The linear relationship between the anodic peak current (i_p) and the square root of scan rate ($v^{1/2}$) demonstrates that the oxidation of N_2H_4 on each of the electrode materials is a

diffusion-limited process (insets in Fig. 4a1–a3 and Fig. S7a1 and a2). In addition, a linear relationship is also found between E_p and the natural logarithm of scan rate ($\lg v$) for all the electrodes (Fig. 4b1–b3 and Fig. S7b1 and b2 in ESI†). For a totally irreversible diffusive process, E_p and i_p can be expressed as^{46,53–55}

$$E_p = \frac{1}{2} \frac{2.3RT}{(1-\alpha)n_\alpha F} \lg v + \text{constant} \quad (5)$$

$$i_p = 3.01 \times 10^5 n[(1-\alpha)n_\alpha]^{1/2} A c D^{1/2} v^{1/2} \quad (6)$$

where α is the electron transfer coefficient, n_α is the electron number in the rate-determining step, n is the total number of electrons involved in the oxidation of N_2H_4 , and other symbols have their usual meanings. On the basis of the electrode areas (A) calculated above, from the slopes of the linear plots E_p – $\lg v$ and i_p – $v^{1/2}$, n was calculated to be 4.07, 3.99, 2.77, 1.12, and 2.01 for the RGO, Cu, L-RGO/Cu, S-RGO/Cu, and H-RGO/Cu electrodes, respectively, using the parameters $R = 8.314$ C mol⁻¹ (Gas constant), $T = 298.18$ K (Room temperature), $F = 96485$ Pa m³ K⁻¹ mol⁻¹ (Faraday constant), $c = 10$ mM, and $D = 2.1 \times 10^{-5}$ cm² s⁻¹ (diffusion coefficient for N_2H_4 ^[30,43,53]). The results demonstrate that anodic oxidation of N_2H_4 on both the RGO and the Cu nanoparticle proceed through a four-electron process as have been reported by others,^[31,43] which means completely electro-oxidation of N_2H_4 on the catalysts to produce only nitrogen according to the chemical formula:^{56,57}



Three-electron, one-electron, and two-electron pathways were obtained for the L-RGO/Cu, S-RGO/Cu, and H-RGO/Cu composites, respectively, which indicates generation of certain products such as hydrogen or ammonia from chemical decomposition of N_2H_4 on the catalysts.⁵⁸ The

hydrogen or ammonia resulted from the N_2H_4 decomposition were not electro-oxidized (as is usually the case on non-noble metals^{58,59}), causing the number of electrons less than 4.⁶⁰

Because of the similar composition and size of the catalyst nanoparticles, the electrocatalytic current density by the RGO/Cu composites depends on the loading of Cu catalyst, the active surface area, and the total electron transfer number involved in the reaction. Due to copper oxide formation and possible dissolution of Cu in the CV fabrication process, determining the amount of Cu deposited from the electrochemical charge consumed is difficult, and consequently the electrocatalytic activities were compared (see Fig. 3) based on qualitative analyses. Generally, the loading of Cu catalyst increases with increasing initial cupreous precursor when the deposition cycles for fabrication are the same. H-RGO/Cu, for example, should contain more Cu particles deduced from the higher initial $[\text{Cu}^{2+}]$ for the H-RGO/Cu preparation and the SEM/TEM observations. On the other hand, the total electron transfer number (two-electron) on H-RGO/Cu is larger than that on S-RGO/Cu (one-electron). So, the lower catalytic current for N_2H_4 oxidation on H-RGO/Cu than that on S-RGO/Cu can exclusively be attributed to the fewer exposed active sites, which are closely related to the small electrochemically effective surface area of H-RGO/Cu (0.265 cm^2) relative to S-RGO/Cu (0.685 cm^2). This agrees with the fact that large electrochemically active surface area of a catalyst contributes to its high electrocatalytic activity. However, little attention has been paid to the correlation between the active surface area and the electrocatalytic mechanism. Here, in view of the total electron transfer numbers the catalytic decomposition reaction of N_2H_4 seems to occur more dominantly than the electro-oxidation reaction with increasing the effective surface area of the anode electrocatalyst through comparing the Cu-containing materials (L-RGO/Cu, S-RGO/Cu, H-RGO/Cu, and the neat Cu nanoparticles). Similar phenomenon was discovered by Yamada and coworkers.⁶¹ Both the complete electro-oxidation pathway and the chemical decomposition pathway can find their uses (for example the former in direct hydrazine fuel cells⁵⁸⁻⁶¹ and the latter in

hydrogen production through N_2H_4 decomposition^{62,63}). This work reveals that the catalyst architecture or rather its active surface area can potentially modulate the electrocatalytic reaction pathways, whereas the control of reaction pathways on electrocatalyst surface has been a challenge.^{64,65} Further, we found that the CV electrodeposition is a general synthetic approach to RGO/metal nanoparticle composites involving the unique layer-by-layer and 3D sandwich-type nanoarchitectures given that the concentration ratios of the metallic precursor to GO are appropriate. This, one hand, confirms our proposed mechanisms about the concentration-dependent electrochemical self-assembly processes. On the other hand, it presents the hope that the precise control over the architecture of selected catalyst compositions using the electrochemical self-assembly method will develop more selective and efficient electrocatalysts, and the studies are under way by us.

3.4 Stability

The stability of the RGO/Cu composites as electrocatalysts for N_2H_4 oxidation was evaluated. The test was carried out using cyclic voltammetry in the potential range of -0.4 – $+0.7$ V at the scan rate of 100 mV s^{-1} in 0.1 M KOH solution containing $10 \text{ mM N}_2\text{H}_4$ (Fig. S8, ESI[†]), and the plots of anodic peak current density versus the number of CV cycles are shown in Fig. 5. It is observed that the electrochemical responses of L-RGO/Cu, S-RGO/Cu, and H-RGO/Cu stabilize after 100 cycles and have the retentions of 81%, 88%, and 67% over 400 consecutive cycles, respectively. We believe that the stability of the RGO/Cu composite electrocatalysts can be further improved by adjusting the structure parameters such as the size of catalyst particles and the thickness of the catalyst layer.

4. Conclusions

We have discovered that the arrangement of RGO sheets in RGO/metal hybrid can be easily regulated using the one-step CV electrodeposition technique. Well-defined layer-by-layer, 3D sandwich-type, and homogeneous structures are obtained for the RGO/Cu composite. In all the three cases, the Cu particles as spacers prevent the restacking of RGO sheets. However, different from the conventional horizontally stacking on conductive substrates, for the first time, we observe that in the 3D sandwich-type RGO/Cu composite, the RGO sheets acting as scaffolds to support Cu nanoparticles growing on their two sides nearly stand on the electrode. Such an architecture should be paid more attention because of the open structure and highly exposed catalytic sites, which indeed endow the RGO/Cu with excellent electrocatalytic activity to N_2H_4 oxidation in the alkaline electrolyte in terms of a higher current density and lower overpotential. Also note that increasing the surface area of catalysts may alter the reaction pathway. This work not only explores a simple electrochemical method for designing well-controlled architectures of multifunctional graphene/metal nanocomposites, but also offers insight into the structure-performance-catalytic mechanism relationships which can guide the development of more efficient and selective electrocatalysts.

Acknowledgements

This work was supported by Excellent Youth Foundation of Hunan Scientific Committee (14JJ1015), the National Natural Science Foundation of China (51202065, 51178173, 51078129), and Program for Innovation Research Team in University (IRT1238).

Notes and references

^a State Key Laboratory of Chemo/Biosensing and Chemometrics, Hunan University, Changsha 410082, P. R. China. E-mail: chem_cbliu@hnu.edu.cn; sllou@hnu.edu.cn

^b College of Materials Science and Engineering, Hunan University, Changsha 410082, P. R. China

† Electronic Supplementary Information (ESI) available: [Raman spectra, XPS, CV curves for electrodeposition, and electrochemical tests are included]. See DOI: 10.1039/b000000x/

References

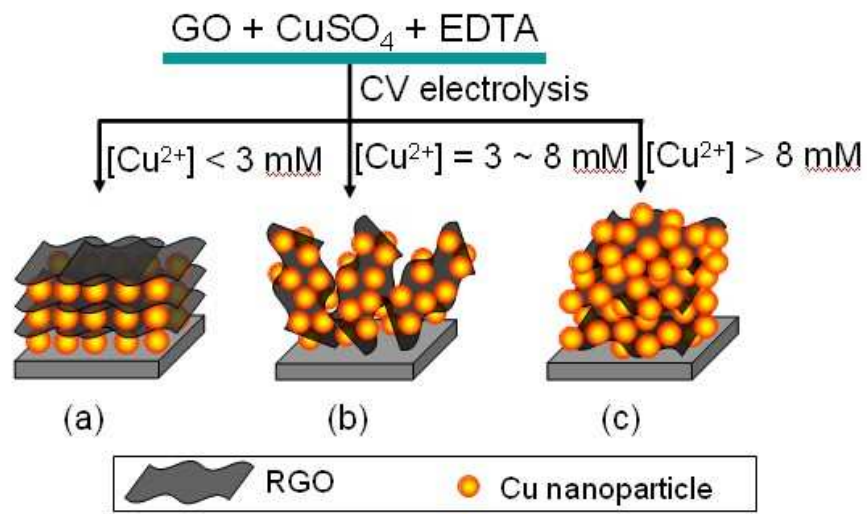
1. C. M. Welch and R. G. Compton, *Anal. Bioanal. Chem.*, 2006, **384**, 601.
2. M. K. Debe, *Nature*, 2012, **486**, 43.
3. A. Chen and P. Holt-Hindle, *Chem. Rev.*, 2010, **110**, 3767.
4. Y. J. Wang, D. P. Wilkinson and J. Zhang, *Chem. Rev.*, 2011, **111**, 7625.
5. S. Sharma and B. G. Pollet, *J. Power Sources*, 2012, **208**, 96.
6. N. Menzel, E. Ortel, R. Kraehnert and P. Strasser, *ChemPhysChem*, 2012, **13**, 1385.
7. Y. Li, Z. Y. Fu and B. L. Su, *Adv. Funct. Mater.*, 2012, **22**, 4634.
8. E. Yoo, T. Okata, T. Akita, M. Kohyama, J. Nakamura and I. Honma, *Nano Lett.*, 2009, **9**, 2255.
9. E. Antolini, *Appl. Catal. B: Environ.*, 2012, **123**, 52.
10. A. K. Geim and K. S. Novoselov, *Nat. Mater.*, 2007, **6**, 183.
11. M. Pumera, A. Ambrosi, A. Bonanni, E. L. K. Chng and H. L. Poh, *Trends Anal. Chem.*, 2010, **29**, 954.
12. C. Xu, X. Wang and J. W. Zhu, *J. Phys. Chem. C*, 2008, **112**, 19841.
13. M. M. Liu, Y. Z. Lu and W. Chen, *Adv. Funct. Mater.*, 2013, **23**, 1348.
14. C. G. Hu, H. H. Cheng, Y. Zhao, Y. Hu, Y. Liu, L. M. Dai and L. T. Qu, *Adv. Mater.*, 2012, **24**, 5493.
15. L. X. Ding, A. L. Wang, G. R. Li, Z. Q. Liu, W. X. Zhao, C. Y. Su and Y. X. Tong *J. Am. Chem. Soc.*, 2012, **134**, 5730.
16. A. Klokke, C. Köhler, R. Gerwig, R. Zengerle and S. Kerzenmacher, *Adv. Mater.*, 2012, **24**, 2916.
17. L. X. Ding, A. L. Wang, G. R. Li, Z. Q. Liu, W. X. Zhao, C. Y. Su and Y. X. Tong, *J. Am. Chem. Soc.*, 2012, **134**, 5730.

18. L. Y. Chen, Y. H. Tang, K. Wang, C. B. Liu and S. L. Luo, *Electrochem. Commun.*, 2011, **13**, 133.
19. C. B. Liu, Y. R. Teng, R. H. Liu, S. L. Luo, Y. H. Tang, L. Y. Chen and Q. Y. Cai, *Carbon*, 2011, **49**, 5312.
20. C. B. Liu, K. Wang, S. L. Luo, Y. H. Tang and L. Y. Chen, *Small*, 2011, **7**, 1203.
21. Y. H. Tang, N. Wu, S. L. Luo, C. B. Liu, K. Wang and L. Y. Chen, *Macromol. Rapid. Commun.*, 2012, **33**, 1780.
22. X. L. Zhang, Y. H. Tang, Y. Li, Y. Wang, X. N. Liu, C. B. Liu and S. L. Luo, *Appl. Catal. B: General*, 2013, **457**, 78.
23. S. L. Yang, J. S. Liang, S. L. Luo, C. B. Liu and Y. H. Tang, *Anal. Chem.*, 2013, **85**, 7720.
24. Y. Y. Jiang, Y. Z. Lu, F. H. Li, T. S. Wu, L. Niu and W. Chen, *Electrochem. Commun.*, 2012, **19**, 21.
25. G. P. Kim, I. Nam, N. D. Kim, J. Park, S. Park and J. Yi, *Electrochem. Commun.*, 2012, **22**, 93.
26. M. Hilder, O. Winther-Jensen, B. Winther-Jensen and D. R. MacFarlane, *Phys. Chem. Chem. Phys.*, 2012, **14**, 14034.
27. D. Wang, W. Yan, S. H. Vijapur and G. G. Botte, *Electrochim. Acta*, 2012, **89**, 732.
28. J. Luo, S. S. Jiang, H. Y. Zhang, J. Q. Jiang and X. Y. Liu, *Anal. Chem. Acta*, 2012, **709**, 47.
29. Y. C. Chou, C. Y. Tai, J. F. Lee, T. S. Chan and J. M. Zen, *Electrochim. Acta*, 2013, **104**, 104.
30. H. C. Gao, Y. X. Wang, F. Xiao, C. B. Ching and H. W. Duan, *J. Phys. Chem. C*, 2012, **116**, 7719.
31. F. L. Jia, J. H. Zhao and X. X. Yu, *J. Power Sources*, 2012, **222**, 135.
32. X. B. Ge, L. Y. Chen, J. L. Kang, T. Fujita, A. Hirata, W. Zhang, J. H. Jiang and M. W. Chen, *Adv. Funct. Mater.*, 2013, **23**, 4156.
33. M. A. Zaitoun and C. T. Lin, *J. Phys. Chem., B* 1997, **101**, 1857.

34. K. Jasuja and V. Berry, *ACS Nano*, 2009, **3**, 2358.
35. G. Goncalves, P. A. Marques, C. M. Granadeiro, H. I. Nogueira, M. Singh and J. Grácio, *Chem. Mater.*, 2009, **21**, 4796.
36. S. B. Yang, X. L. Feng, L. Wang, K. Tang, J. Maier and K. Müllen, *Angew. Chem. Int. Ed.*, 2010, **49**, 4795.
37. J. J. Xu, K. Wang, S. Z. Zu, B. H. Han and Z. X. Wei, *ACS Nano*, 2010, **4**, 5019.
38. R. G. Cao, J. S. Lee, M. L. Liu and J. Cho, *Adv. Energy Mater.*, 2012, **2**, 816.
39. G. L. Che, B. B. Lakshmi, E. R. Fisher and C. R. Martin, *Nature*, 1998, **393**, 346.
40. Z. H. Ai, L. Z. Zhang, S. C. Lee and W. Ho, *J. Phys. Chem. C*, 2009, **113**, 20896.
41. A. Radi, D. Pradhan, Y. Sohn and K. Leung, *ACS Nano*, 2010, **4**, 1553.
42. G. Karim-Nezhad, R. Jafarloo and P. S. Dorraji, *Electrochim. Acta*, 2009, **54**, 5721.
43. Y. Wang, Y. Wan and D. Zhang, *Electrochem. Commun.*, 2010, **12**, 187.
44. F. G. Xu, Y. J. Sun, Y. Zhang, Y. Shi, Z. W. Wen and Z. Li, *Electrochem. Commun.*, 2011, **13**, 1131.
45. I. V. Lightcap, T. H. Kosel and P. V. Kamat, *Nano lett.*, 2010, **10**, 577.
46. A. J. Bard and L. R. Faulkner, *Electrochemical Methods: Fundamentals and Applications*, John Wiley, New York 2001.
47. L. L. Zhang, R. Zhou and X. S. Zhao, *J. Mater. Chem.*, 2010, **20**, 5983.
48. C. H. Xu, B. H. Xu, Y. Gu, Z. G. Xiong, J. Sun and X. S. Zhao, *Energy Environ. Sci.*, 2013, **6**, 1388.
49. W. Xing, S. Z. Qiao, R. G. Ding, F. Li, G. Q. Lu, Z. F. Yan and H. M. Cheng, *Carbon*, 2006, **44**, 216.
50. W. G. Pell and B. E. Conway, *J. Electroanal. Chem.*, 2001, **500**, 121.
51. C. C. Hu and T. W. Tsou, *Electrochem. Commun.*, 2002, **4**, 105.

52. H. L. Li, J. X. Wang, Q. X. Chu, Z. Wang, F. B. Zhang and S. C. Wang, *J. Power Sources*, 2009, **190**, 578.
53. J. Li and X. Q. Lin, *Sens. Actuators B*, 2007, **126**, 527.
54. J. A. Harrison and Z. A. Khan, *J. Electroanal. Chem.*, 1970, **28**, 131.
55. S. M. Golabi and H. R. Zare, *J. Electroanal. Chem.*, 1999, **465**, 168.
56. H. M. Nassef, A. E. Radi and C. K. O'Sullivan, *J. Electroanal. Chem.*, 2006, **592**, 139.
57. S. J. Lao, H. Y. Qin, L. Q. Ye, B. H. Liu and Z. P. Li, *J. Power Sources*, 2010, **195**, 4135.
58. K. Yamada, K. Yasuda, H. Tanaka, Y. Miyazaki and T. Kobayashi, *J. Power Sources*, 2003, **122**, 132.
59. J. Sanabria-Chinchilla, K. Asazawa, T. Sakamoto, K. Yamada, H. Tanaka and P. Strasser, *J. Am. Chem. Soc.*, 2011, **133**, 5425.
60. K. Asazawa, T. Sakamoto, S. Yamaguchi, K. Yamada, H. Fujikawa, H. Tanaka and K. Oguro, *J. Electrochem. Soc.*, 2009, **156**, B509.
61. K. Yamada, K. Asazawa, K. Yasuda, T. Ioroi, H. Tanaka, Y. Miyazaki and T. Kobayashi, *J. Power Sources*, 2003, **115**, 236.
62. J. Wang, X. B. Zhang, Z. L. Wang, L. M. Wang and Y. Zhang, *Energy Environ. Sci.*, 2012, **5**, 6885.
63. S. K. Singh and Q. Xu, *Catal. Sci. Technol.*, 2013, **3**, 1889.
64. A. Rabis, P. Rodriguez and T. J. Schmidt, *ACS Catal.*, 2012, **2**, 864.
65. A. A. Gewirth and M. S. Thorum, *Inorg. Chem.*, 2010, **49**, 3557.

Inserting Graphics



Scheme 1 Fabrication processes for the RGO/Cu composite, obtaining (a) layer-by-layer, (b) sandwich-type, and (c) homogeneous structures depending on the initial concentrations of the cupreous precursor.

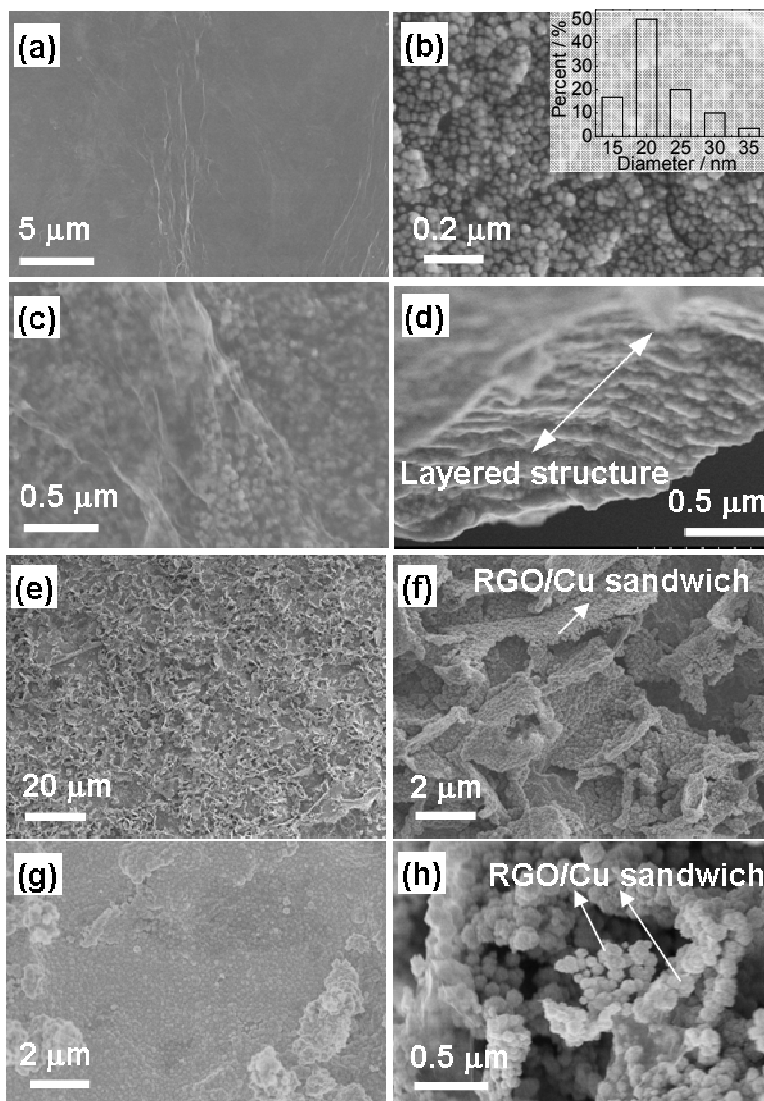
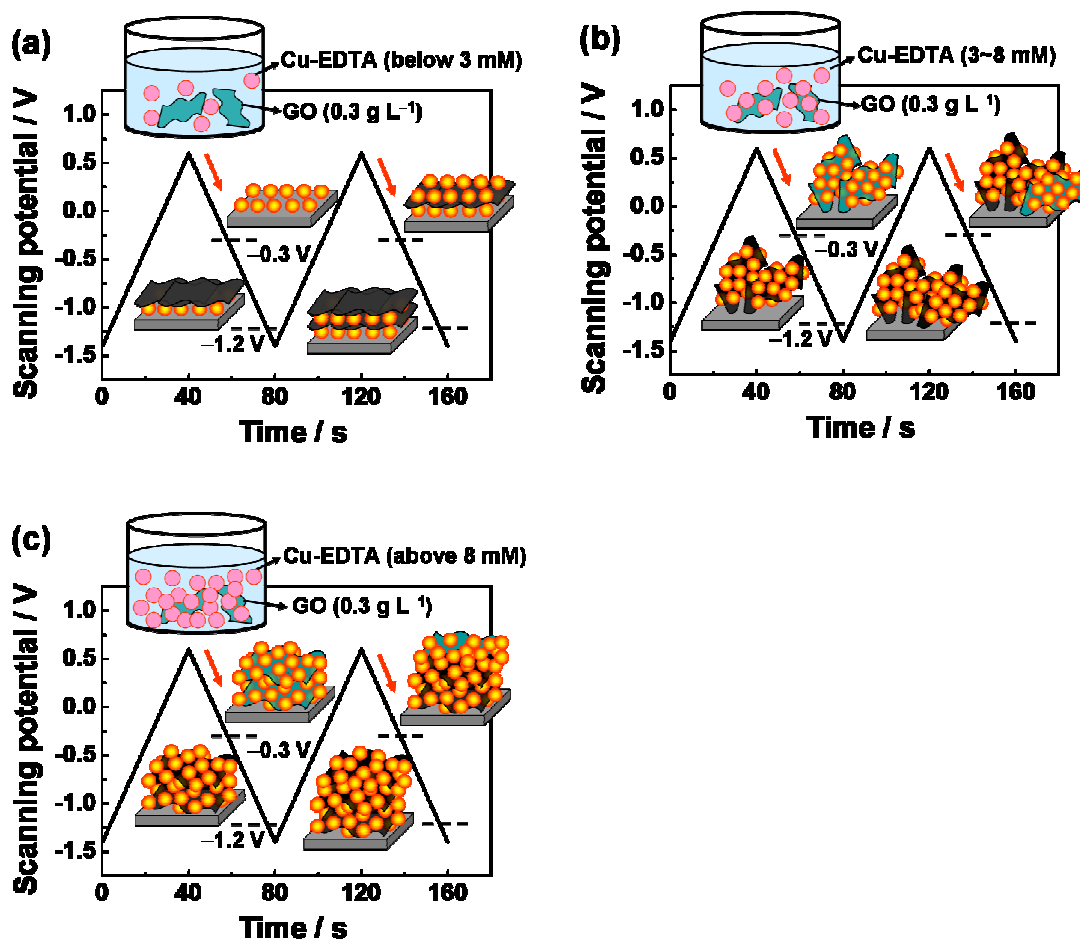


Fig. 1 Typical top-view SEM images of (a) RGO, (b) Cu nanoparticles with diameter distribution inset, (c) L-RGO/Cu, (e, f) S-RGO/Cu, and (g) H-RGO/Cu. (d) and (h) are cross-sectional SEM images of (c) and (g), respectively.



Scheme 2 Electrochemical self-assembly mechanisms for (a) layer-by-layer, (b) sandwich-type, and (c) homogeneous RGO/Cu composites during the CV scanning between -1.4 and 0.6 V.

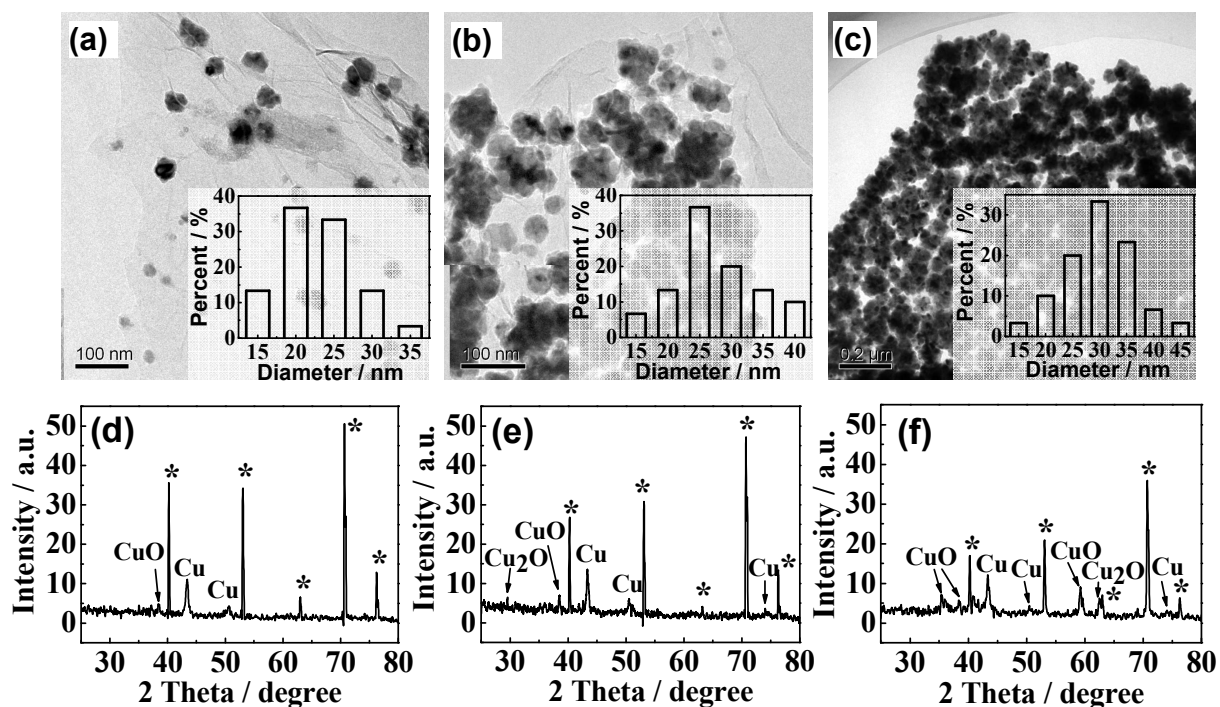


Fig. 2 TEM images and particle size distributions of (a) L-RGO/Cu, (b) S-RGO/Cu, and (c) H-RGO/Cu. (d–f) XRD patterns for L-RGO/Cu, S-RGO/Cu, and H-RGO/Cu, respectively. The samples for XRD characterization were electrodeposited on Ti foils and the diffraction peaks marked with * come from the Ti substrate (JCPDS file no. 05-0682).

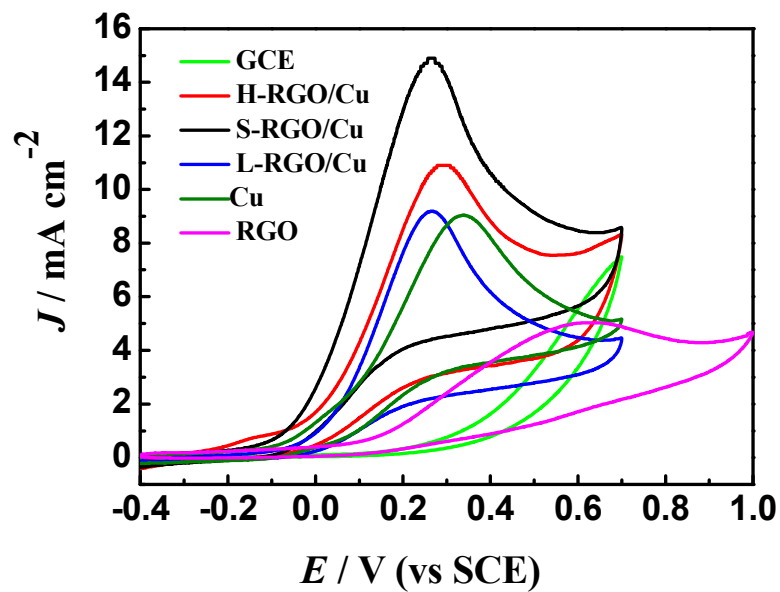


Fig. 3 Cyclic voltammograms at a bare GCE and the GCEs loaded with RGO, Cu, L-RGO/Cu, S-RGO/Cu, and H-RGO/Cu in 0.1 M KOH containing 10 mM hydrazine at the scan rate of 100 mV s^{-1} .

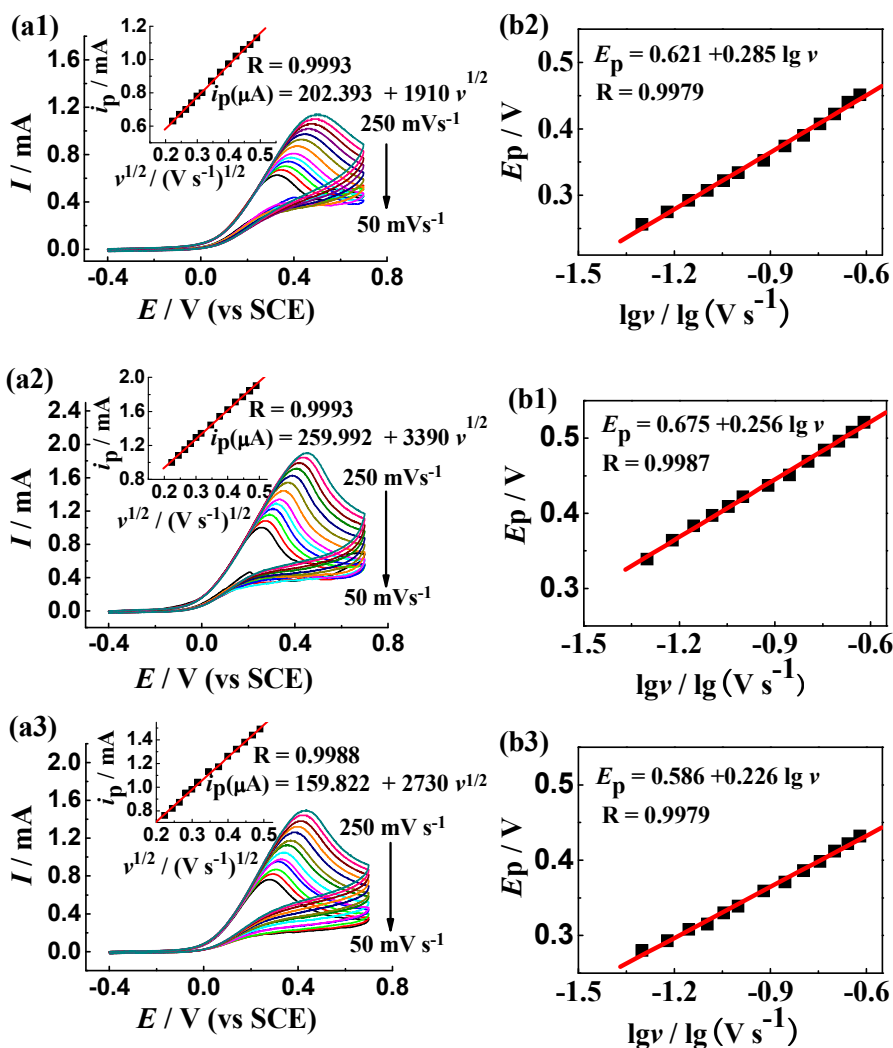


Fig. 4 Cyclic voltammograms at the GCEs loaded with (a1) L-RGO/Cu, (a2) S-RGO/Cu, and (a3) H-RGO/Cu in 0.1 M KOH containing 10 mM hydrazine at various scan rates of 50, 60, 70, 80, 90, 100, 120, 140, 160, 180, 200, and 250 mV s^{-1} . Insets represent the dependence of the peak current (i_p) on the square root of the scan rate ($v^{1/2}$). (b1)–(b3) represent the dependence of the peak potential (E_p) in (a1)–(a3), respectively, on the natural logarithm of the scan rate ($\lg v$).

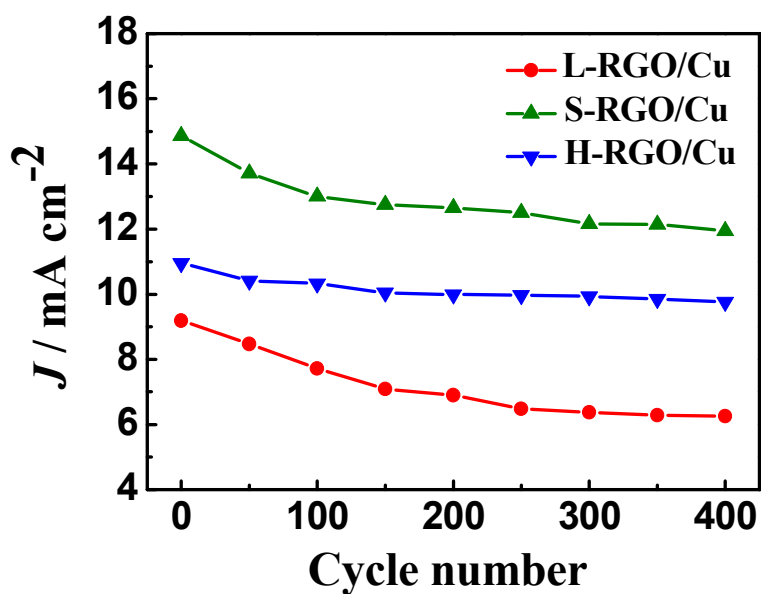


Fig. 5 Plots of anodic peak current density versus the number of CV cycles, where the anodic peak currents were acquired from the cyclic voltammograms of the RGO/Cu composites loaded GCEs in the potential range of -0.4 – $+0.7$ V at the scan rate of 100 mV s^{-1} in 0.1 M KOH solution containing 10 mM hydrazine.